RESEARCH ARTICLE

Check for updates

Ternary PtVCo dendrites for the hydrogen evolution reaction, oxygen evolution reaction, overall water splitting and rechargeable Zn–air batteries†

Zhaoqing Ding,[a] Zhenghua Tang, [ID] *[a,b] Ligui Li, [ID][a,b] Kai Wang,[a] Wen Wu,[a] Xiaoning Chen,[a] Xiao Wu[a] and Shaowei Chen [ID][a,c]

Designing a highly active, robust and cost-effective electrocatalyst with multiple functionalities toward overall water splitting and rechargeable Zn–air battery applications is crucial and urgent for the development of sustainable energy sources. Herein, we report the one-step facile fabrication of ternary PtVCo alloyed dendrites as highly efficient bifunctional catalysts for both the hydrogen evolution reaction (HER) and oxygen evolution reaction (OER), as well as their deployment for both overall water splitting and rechargeable Zn–air batteries. Their HER activity and long-term durability were superior to those of commercial Pt/C, and their OER performance was close to that of the standard IrO_2 catalyst. The PtVCo modified electrode can catalyze water splitting very efficiently. Furthermore, in the self-assembled rechargeable Zn–air battery test, PtVCo exhibited a narrow charge–discharge voltage gap of 0.88 V and a maximal power density of 235 mW cm^{-2}, which outperformed the performance of Pt/C. The excellent performance of PtVCo is mainly attributed to the synergistic contributions from Pt, V and Co, as the introduction of two transition metals significantly alters the electronic structure and the surface local ordering arrangements.
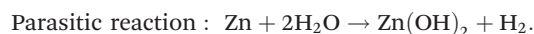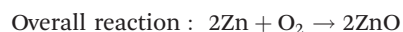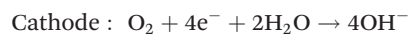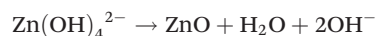
Introduction

Recently, intensive research efforts on developing efficient, non-toxic and inexpensive energy conversion and storage technologies have been provoked by the rapidly growing demand for clean and renewable energy sources. Among those, hydrogen has been widely considered as one of the most promising green sources of energy thanks to its high energy density and non-toxic nature.[1–3] Among all kinds of hydrogen production approaches, electrochemical overall water spitting is an effective means to generate hydrogen with high purity, but its reaction kinetics is largely hindered by the lack of efficient and highly active bifunctional electrocatalysts to reduce the overpotential for both the hydrogen evolution reaction (HER) and oxygen evolution reaction (OER).[4–6] Meanwhile, rechargeable Zn–air batteries (ZABs) have demonstrated great promise to be employed in portable devices, electric vehicles and other utility-scale energy devices due to their safety, low cost, environmental friendliness and high theoretical energy density.[7–9] The reactions occurring at ZABs can be summarized by the following equations:[9]

$$\text{Anode}: \ \text{Zn} + 4\text{OH}^- \rightarrow \text{Zn(OH)}_4{}^{2-} + 2e^-$$

$$\text{Zn(OH)}_4{}^{2-} \rightarrow \text{ZnO} + \text{H}_2\text{O} + 2\text{OH}^-$$

$$\text{Cathode}: \ \text{O}_2 + 4e^- + 2\text{H}_2\text{O} \rightarrow 4\text{OH}^-$$

$$\text{Overall reaction}: \ 2\text{Zn} + \text{O}_2 \rightarrow 2\text{ZnO}$$

$$\text{Parasitic reaction}: \ \text{Zn} + 2\text{H}_2\text{O} \rightarrow \text{Zn(OH)}_2 + \text{H}_2.$$
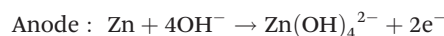
The OER and oxygen reduction reaction (ORR) are two prominent reactions involved in ZABs, which represent the charging and discharging process, respectively, hence determining the practical performance of the ZABs.[8,10,11] To this end, devel-

[a]*Guangzhou Key Laboratory for Surface Chemistry of Energy Materials, New Energy Research Institute, School of Environment and Energy, South China University of Technology, Guangzhou Higher Education Mega Centre, Guangzhou, 510006, P. R. China. E-mail: zhht@scut.edu.cn*
[b]*Guangdong Provincial Key Laboratory of Atmospheric Environment and Pollution Control, Guangdong Engineering and Technology Research Center for Environmental Nanomaterials, South China University of Technology, Guangzhou Higher Education Mega Centre, Guangzhou, 510006, P. R. China*
[c]*Department of Chemistry and Biochemistry, University of California, 1156 High Street, Santa Cruz, California 95064, USA*
†Electronic supplementary information (ESI) available: The procedure for Zn–air battery measurements, additional tables, SEM images, HR-TEM images, XPS survey scan spectra, additional cyclic voltammograms and linear sweep voltammograms. See DOI: 10.1039/c8qi00623g

This journal is © the Partner Organisations 2018

Inorg. Chem. Front., 2018, **5**, 2425–2431 | **2425**

oping efficient and robust electrocatalysts as an air-cathode is of paramount importance to enhance the sluggish kinetics of the OER and ORR,[12–15] to attain a high power density and long lifecycle of ZABs eventually. Currently, Pt/C is the state-of-art electrocatalyst for the HER[16] and ORR,[17] while IrO$_2$/RuO$_2$ is the standard catalyst for the OER,[18] where all of them are noble metal-based materials, hence being significantly hampered by the high cost due to their low earth abundance. These catalysts also suffer from other disadvantages such as sluggish reaction kinetics, poor long-term stability, low poison resistance and so on.[19,20] Therefore, to fully realize the potential of overall water splitting, seeking active bifunctional electrocatalysts for both the HER and OER to operate in the same electrolyte is highly desirable.[21,22] Meanwhile, developing a cheap, stable and efficient bi-functional electrocatalyst for both the OER and ORR is non-negotiable for the large-scale implementation of ZABs.[9,10,12,13,23,24]

To lower the cost and increase the intrinsic activity toward electrocatalytic reactions, one effective strategy is alloying noble metals with transition metals. For instance, PtM (M = transition metals such as Fe, Co, Ni etc.) alloys have displayed enhanced electrocatalytic activity compared to pure Pt based materials due to the introduction of synergistic catalytic effects.[25–27] Computational studies also revealed that the transition metal in the alloys can significantly tune the electronic properties and the atomic ordering environment, hence playing a significant role in the electrochemical process.[28–30] Recently, ternary alloys of PtMM′ (M and M′ = Fe, Co, Ni etc.) electrocatalysts have been gaining increasing research attention, due to the introduction of additional synergistic effects, the possibility of realizing precise manipulation of the surface atomic ordering structure, and the significant enhancement of the chemical and thermal stability under harsh operation conditions toward real applications.[31] By using engineered PtVFe nanoparticles with a controlled composition and size supported on carbon as cathode electrocatalysts, the Zhong group found that PtVFe as a membrane electrode assembly for proton exchange membrane fuel cells (PEMFCs) possessed excellent performance comparable to commercial Pt/C.[32] Guo et al. prepared PtNiFe dandelion-like alloys for the methanol oxidation reaction (MOR), which exhibited high activity and poison tolerance with remarkable durability.[33] In 2015, the Smirnova group reported the preparation of PtIrCo-alloy nanoparticles impregnated into a carbon aerogel matrix, which showed better CO-tolerant MOR and methanol-resistant ORR activity compared to the Pt-catalyst.[34] Recently, Sriphathoorat et al. have successfully synthesized well-defined PtNiCo dendrites with improved activity toward the MOR compared to commercial Pt/C, and the PtNiCo ternary alloys presented a dendritic structure composed of a Pt–Ni–Co core and a dendritic Pt–Co bimetallic shell.[35]

Herein, we report the one-step facile synthesis of PtVCo alloys, and electron microscopy studies revealed a dendrite structure with a rough surface. Binary PtV and PtCo alloys have also been prepared as the control samples. In the electrochemical tests, the HER performance of PtVCo was superior to that of PtV, PtCo and Pt/C. Also, its OER performance was close to that of IrO$_2$ and much better than that of PtV and PtCo, which made it eventually being employed to catalyze overall water splitting very efficiently. PtVCo exhibited superior HER and OER performance to binary PtV and PtCo alloys, which can be attributed to the synergistic contributions from Pt, V and Co, as well as the as-formed characteristic dendrite structure. In the preliminary rechargeable Zn–air battery tests, PtVCo exhibited a narrow charge–discharge voltage gap of 0.88 V and a maximal power density of 235 mW cm^{-2}, which outperformed those of commercial Pt/C. It is worth noting that all the performances were tested in alkaline electrolytes and the HER performance of PtVCo in 1 M KOH was even superior to that of commercial Pt/C.

Experimental section

Materials

Platinum bis(acetylacetonate) (Pt(acac)$_2$, 98%), vanadyl acetylacetonate (VO(acac)$_2$, 99%), tris(2,4-pentanedionato) cobalt(III) (Co(acac)$_3$, 98%), oleylamine (OAM, 80%-90%), N-hexadecyltrimethylammonium chloride (CTAC, 99%) and iridium oxide (IrO$_2$, 98%) were purchased from Energy Chemicals (Shanghai, China). Absolute ethanol (99.7%), potassium hydroxide (KOH, ≥85.0%) and zinc acetate dehydrate (ZnAc·2H$_2$O, ≥99.0%) were obtained from Damao Chemical Reagents (Tianjin, China) and n-hexane (98.0%) was acquired from Zhiyuan Chemical Reagents (Tianjin, China). Commercial 20 wt% Pt/C was acquired from Alfa Aesar. Nafion (5 wt%) was obtained from Kunshan Yiercheng (Suzhou, China). Water was offered by a Barnstead Nanopure Water System (18.3 MΩ cm). All chemicals were used as received without further purification.

Preparation of the PtVCo ternary alloy

Typically, 10.6 mg Pt(acac)$_2$, 8.0 mg VO(acac)$_2$ and 7.3 mg Co(acac)$_3$ were co-dissolved in 10 mL OAM, and then 120 mg CTAC was added into the above mixture. After sonication for 20 min, the homogeneous solution was solvothermally treated in a 25 mL Teflon-lined stainless steel autoclave at 200 °C for 18 h and cooled down to ambient temperature. Subsequently, the resulting products were washed by using a mixture of ethanol/hexane 3–5 times and the leftover solid was the as-obtained PtVCo sample. PtV and PtCo were prepared in a similar manner.

Characterization

The morphologies and surface structures of the samples were observed by field-emission scanning electron microscopy (SEM, Hitachi S-4800) and transmission electron microscopy (TEM, Tecnai G2 F30). X-ray diffraction (XRD) patterns in the Bragg's angle (2θ) ranging from 10 to 90° were obtained by using a Bruker D8 diffractometer with Cu Kα radiation (λ = 0.1541 nm). X-ray photoelectron spectroscopy (XPS) was con-

2426 | Inorg. Chem. Front., 2018, 5, 2425–2431

This journal is © the Partner Organisations 2018

ducted by using an Escalab 250 photoelectron spectrometer (Thermo Fisher Scientific, USA).

Electrochemical Measurements

Electrochemical measurements were carried out with a CHI 750E electrochemical workstation (CH Instruments Inc.) at ambient temperature. The HER was performed in 1 M KOH aqueous solution. An AgCl/Ag electrode ($E_{AgCl/Ag} = E_{RHE} - 1.023$ V) and a carbon rod (diameter 3.0 mm) were employed as the reference electrode and the counter electrode, respectively. A glass carbon electrode (acreage 0.07 cm^2) was used as the working electrode. Firstly, 2 mg of the catalyst was dispersed in 1 mL absolute ethanol with 20 μL Nafion to make a homogeneous catalyst ink. The catalyst ink (10 μL) was then added dropwise onto the working electrode and dried naturally, and the catalyst loading was calculated to be 0.286 mg cm^{-2} for all samples. LSV measurements were conducted in the potential range of −0.477 V to +0.323 V (vs. RHE) with a scan rate of 10 mV s^{-1}. For the OER, a platinum plate and a rotating ring disk electrode (RRDE) (diameter 5.0 mm) were employed as the counter electrode and the working electrode, respectively. The RRDE was mechanically polished with aqueous slurries of 0.5 μm alumina powders. The catalyst loading was approximately 0.102 mg cm^{-2}. The LSV curves of the OER were recorded in a N$_2$-saturated 1 M KOH solution at 1600 rpm within the potential range of +1.023 V to +2.023 V (vs. RHE) with a scan rate of 10 mV s^{-1}. Water splitting tests were conducted by following a similar procedure to the OER test but the potential range was set from −0.477 V to +2.023 V (vs. RHE). For the ORR test, the LSV measurements were performed in an O$_2$-saturated 0.1 M KOH solution at 1600 rpm in the potential range of −0.036 V to +1.164 V (vs. RHE) with a scan rate of 10 mV s^{-1}. Cyclic voltammetric (CV) measurements were performed within the potential range of −0.036 V to +1.164 V (vs. RHE). Chronoamperometric responses for the OER were recorded in 1 M KOH at +1.613 V (vs. RHE) for 40 000 s, and accelerated durability tests (ADT) for the HER were carried out by cycling the catalyst over the potential range of −0.127 V to +0.073 V for 3000 cycles with a scan rate of 50 mV s^{-1} in 1 M KOH solution.

Zn–air battery test

The primary rechargeable Zn–air battery was self-fabricated and self-assembled. The air-cathode for the primary Zn–air battery was prepared by coating the catalyst ink onto a hydrophobic carbon cloth and assessed in 6 M KOH electrolyte containing 0.2 M ZnAc. All Zn–air battery data were acquired by using the CHI-440 electrochemical workstation (CH Instruments Inc.) at room temperature. The experimental details can be found in the ESI.†

Results and discussion

The morphology and surface structural feature of the as-prepared PtVCo sample were first observed by electron microscopy
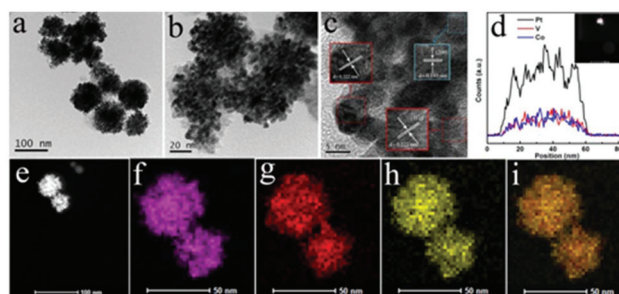

Fig. 1 Representative TEM image (a), (b) and HR-TEM image (c) of the PtVCo sample. Cross-section compositional line-scan profile (d) of PtVCo (inset: a typical HAADF-STEM image). Typical black field (BF)-STEM image (e) of the PtVCo sample and the EDX elemental mapping of Pt (f), V (g), Co (h) and Pt + V + Co (i) elements in the PtVCo sample.

techniques. The typical SEM images of PtVCo can be found in Fig. S1,† and aggregated spherical particles with a rough surface can be observed for PtVCo. Fig. 1a and b present the representative TEM images of PtVCo with different magnifications. It shows a dendrite shape, with some particles clustered together. It can be noted that there are various protrusions and sags in the dendrite structure, and previous reports have documented that such an architecture can significantly enhance the active sites and be favorable for electrocatalytic reactions.[27,35–37] From the typical high-resolution (HR) TEM image (Fig. 1c), one may notice that well-defined lattice spaces can be easily identified. The approximate diameter of an individual dendrite can be estimated as ~75.8 ± 25.0 nm. The d-spacing of 0.222 nm and 0.193 nm can be ascribed to the crystal planes of Pt (111) and Pt (200),[36,38] respectively. Subsequently, high-angle angular dark field scanning tunneling transmission electron microscopy (HAADF-STEM) is performed to disclose the elemental distribution of the PtVCo composite. As shown in Fig. 1d, from an individual dendrite (inset), the line-scan profile can be extrapolated, where both V and Co exhibit almost identical content that is lower than that of Pt. However, the three elements demonstrate a similar distribution trend, indicating the formation of a PtVCo ternary alloy. The typical bright-field (BF) STEM image of PtVCo is illustrated in Fig. 1e. The EDX mapping from Fig. 1f–i further shows that the three elements Pt, V and Co are well mixed with a uniform distribution, further attesting the formation of the ternary alloy. The representative TEM images of PtV and PtCo can be found in Fig. S2.† A similar dendrite shape with less-defined features can be observed for PtV, while aggregation occurred heavily in PtCo alloys. Such slight or heavy aggregation phenomena in PtV and PtCo alloys can significantly decrease the electrochemically active sites, hence substantially impairing the corresponding electrocatalytic performance.

The crystalline nature of PtVCo was next probed by X-ray diffraction (XRD). As illustrated in Fig. 2a, for PtV and PtCo, a series of Bragg reflections can be readily recognized, which correspond well with the reported patterns of the (111), (200), (220), and (311) crystal phases of Pt$_3$V and Pt$_3$Co.[27,39]
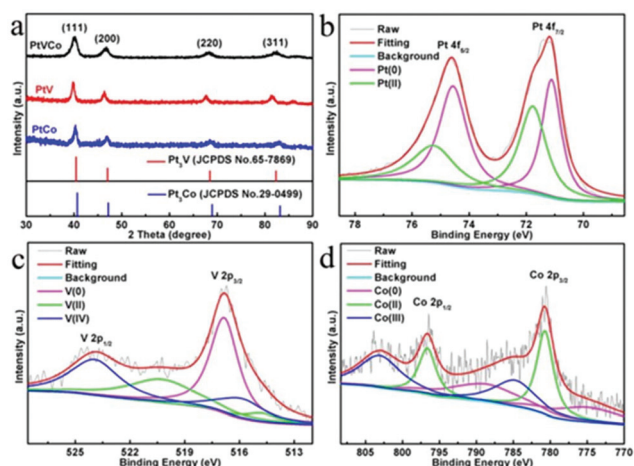
Fig. 2 (a) XRD patterns of the PtVCo, PtV, and PtCo alloys. The high-resolution XPS spectra for the (b) Pt 4f electrons, (c) V 2p electrons, and (d) Co 2p electrons in PtVCo alloys. Black curves are experimental data and colored curves are deconvolution fits.

Moreover, the XRD patterns of the ternary PtVCo dendrites can be obviously attributed to the (111), (200), (220), and (311) crystal planes of PtVCo with the 2θ peak positions at 40.15°, 46.77°, 68.26° and 82.36°, respectively. It is noteworthy that the 2θ peak positions of PtVCo are in between PtV and PtCo, and the d value (0.193 nm) of PtVCo (200) also fell between PtV (200) of 0.194 nm and PtCo (200) of 0.192 nm, correspondingly.[35] The results further solidly prove that the ternary PtVCo alloy was formed, in good agreement with the HR-TEM image analysis.[40] In addition, the electronic structures of PtVCo along with the charge state of each element were studied by XPS measurements. The survey scan spectra of PtVCo are shown in Fig. S3,† where the sharp peaks with strong signals from Pt 4f, V 2p and Co 2p electrons confirmed the co-existence of the three elements. Fig. 2b presents the core-level XPS spectra of the Pt 4f electrons, where a pair of peaks with binding energies at 74.6 eV and 71.3 eV can be assigned to the Pt $4f_{5/2}$ and Pt $4f_{7/2}$ electrons. The two peaks can be de-convoluted into two doublets, where the binding energies at 74.5 eV and 71.1 eV are from metallic Pt and the binding energies at 75.2 eV and 71.8 eV are ascribed to oxidized Pt (Pt(II)).[41,42] Based on the integrated area, the calculated percentage of the Pt(0) and Pt(II) was 56.28% and 43.72%, respectively, and Pt(0) dominated the Pt species. Note that Pt(0) has been documented to be favorable for O_2 and H_2 adsorption, hence accelerating the ORR and HER kinetics.[16,41,43] The high-resolution XPS spectra of the V 2p electrons are shown in Fig. 2c, and the peaks with binding energies at 523.8 eV and 516.8 eV can be ascribed to the V $2p_{1/2}$ and V $2p_{3/2}$ electrons, respectively. It is worth noting that the broad peak for the V $2p_{3/2}$ electrons can be deconvoluted into three defined peaks with binding energies at 514.8 eV, 515.9 eV, and 516.9 eV, which can be attributed to V(0), V(II), and V(IV), respectively.[44] In addition, the high-resolution XPS spectra for the Co 2p electrons from PtVCo are shown in Fig. 2d. The Co 2p1/2 and Co 2p3/2 electrons display

peaks with binding energies at 796.7 eV and 780.8 eV, respectively, both of which can be deconvoluted into three peaks. The two peaks with binding energies at 788.7 eV and 775.0 eV are assigned to metallic Co, another two peaks with binding energy at 796.6 eV and 780.7 eV are attributed to Co(II), and the remaining two peaks located at 803.0 eV and 784.8 eV are from Co(III).[45–47] Through the estimation of the integrated peak area, the percentage of Co(0), Co(II) and Co(III) can be calculated approximately as 33.28%, 31.72%, and 35.00%, respectively. The oxidized Co species accounts for the total ratio of 66.72%, and such domination is probably beneficial for the OER performance, as several previous studies have reported that the co-existence of Co(II) and Co(III) can lower the binding energy of different adsorption intermediates (such as OH$^{\bullet}$, OOH$^{\bullet}$, O$^{\bullet}$ and the like) on the catalyst surface and therefore decreases the activation energy barrier to some extent.[48,49]

The electrocatalytic performance toward the HER was first examined and compared with that of the Pt/C catalyst in N_2-saturated 1 M KOH. As shown in the LSV curves from Fig. 3a, the samples of PtVCo, PtV and PtCo exhibited nearly zero onset potential, almost identical to that of Pt/C. However, to afford a current density of 10 mA cm^{-2}, the required over-potential is 92, 58, 64, and 45 mV for PtV, PtCo, Pt/C, and PtVCo, respectively (Table S1†). PtVCo exhibited the best HER activity, higher than their counterparts PtV and PtCo, and the Pt/C catalyst. Fig. 3b presents the Tafel plot of all the samples, from which the Tafel slope can be determined. PtV had the highest Tafel slope value, indicative of the very sluggish kinetics, while PtVCo possessed the lowest Tafel slope, slightly lower than that of Pt/C and PtCo. Such a low Tafel slope suggests a very rapid HER rate, and a Tafel–Volmer mechanism where the reaction rate-determining step was the electrochemical desorption of H_2.[2,50] The electrochemical impedance spectroscopy study
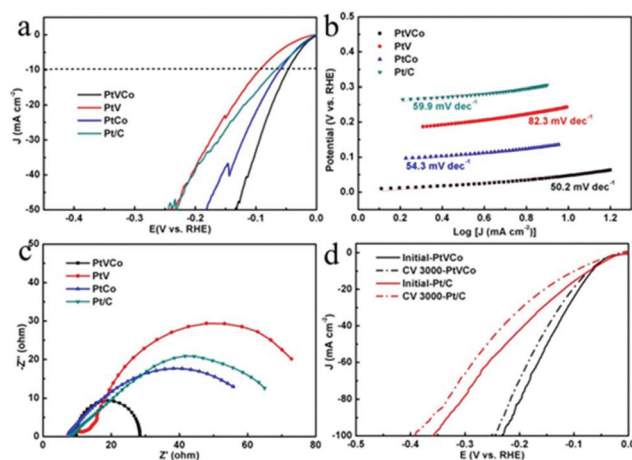

Fig. 3 (a) LSV curves of PtVCo, PtV, PtCo and commercial Pt/C in N_2-saturated 1 M KOH with a scan rate of 10 mV s^{-1}. (b) The corresponding Tafel plot of different catalysts in the HER. (c) Electrochemical impedance spectra of all catalysts for the HER at −0.057 V (vs. RHE). (d) HER polarization curves of PtVCo and Pt/C before and after 3000 cycles in 1 M KOH aqueous solution.

2428 | Inorg. Chem. Front., 2018, 5, 2425–2431

This journal is © the Partner Organisations 2018

was then conducted to further elucidate the reaction kinetics. The Nyquist plot recorded at −0.057 V for a GCE modified with the samples is presented in Fig. 3c. PtV exhibited the largest semicircle, reflecting the inferior HER activity in the series. PtVCo showed the lowest electron transfer resistance, as attested by the smallest semicircle, which also agreed well with the best HER activity among the series. To further compare the HER performance, the long-term stability tests of PtVCo and Pt/C were performed by acquiring the LSV polarization curves before and after 3000 cycles of potential scans. As shown in Fig. 3d, at a current density of 100 mA cm^{-2}, the required over-potential of Pt/C shifted about 34 mV after 3000 cycles in the polarization curve, while in sharp contrast, only a 12 mV negative potential shift was observed for that of PtVCo, suggesting an outperformance compared to that of Pt/C on long-term stability.

In addition to the HER, the electrocatalytic performance of the samples toward the OER was also examined and compared with that of the state-of-the-art IrO$_2$ catalyst. Fig. 4a shows the polarization curves in N$_2$-saturated 1 M KOH. It can be noted that PtV had a barely weak OER activity. To afford a current density of 10 mA cm^{-2}, the required overpotential was 1.64, 1.59, and 1.58 V for PtCo, PtVCo and IrO$_2$ (Table S1†), respectively. PtVCo exhibited superior OER activity to PtCo, close to IrO$_2$. The corresponding Tafel plot of the series samples and IrO$_2$ is presented in Fig. 4b, where PtV exhibited a very high Tafel slope of 179.4 mV dec^{-1} as expected. PtVCo exhibited a lower Tafel slope than PtCo, close to that of IrO$_2$. It indicates that a fast OER kinetics was adopted for PtVCo, comparable to IrO$_2$. To further elucidate the reaction kinetics, the electrochemical impedance spectroscopy investigation was conducted. As shown in Fig. 4c, PtV exhibited a near-linear line in

the wide frequency range, in echo with its negligible OER activity. Besides that, PtVCo displayed a smaller semi-circle than PtCo, indicating a lower electron transfer resistance. However, its resistance was still larger than that of IrO$_2$, corresponding well with the OER performance. Finally, the long-term durability toward the OER for PtVCo was tested and compared with IrO$_2$. From the chronoamperometric i–t curves in Fig. 4d, one can see that, upon continuous operation of 11 h, PtVCo can retain 78.8% of its initial current, while only 39.1% initial value of IrO$_2$ can be preserved. The results suggested that PtVCo had a remarkably higher long-term stability than IrO$_2$ for the OER.

To further probe the bifunctional electrocatalytic properties of the PtVCo sample, its combined OER and HER behaviours were examined and compared with those of Pt/C and IrO$_2$ in 1 M KOH solution (Fig. 5a). For the HER part on the left, IrO$_2$ barely exhibited HER activity, and at a current density of 10 mA cm^{-2}, the overpotential of PtVCo was 31 mV, smaller than that of PtV, PtCo and Pt/C as well. For the OER part on the right, both PtV and Pt/C had a very weak OER activity. To reach a current density of 10 mA cm^{-2}, the required overpotential was 1.61 V, smaller than that of PtCo, close to the benchmark IrO$_2$ catalyst. The comparison of the samples with the combined HER and OER behaviours is summarized in Table S2.† Obviously, to achieve a current density of 10 mA cm^{-2} at both HER and OER terminals for the overall water splitting, PtVCo possessed the lowest voltage gap, smaller than that of PtCo, PtV and Pt/C as well, showing the most promising water-splitting capability among the series. Moving forward to practical applications, a two-electrode electrolyzer using PtVCo was self-assembled to evaluate its performance for overall water splitting in 1 M KOH. As presented in Fig. 5b, when applying a potential of 1.7 V, discernible gas bubbles on the surface of both the cathode and anode can be observed. The generation of H$_2$ at the anode was much faster than that at the cathode for O$_2$, which can be ascribed to the much higher solubility of O$_2$ in water than H$_2$ and the lower reaction rate in O$_2$ formation.[51]

Besides HER and OER tests, the catalytic performance toward the ORR for the series of samples was also evaluated in O$_2$-saturated 0.1 M KOH solution (Fig. S4†). The CV and LSV
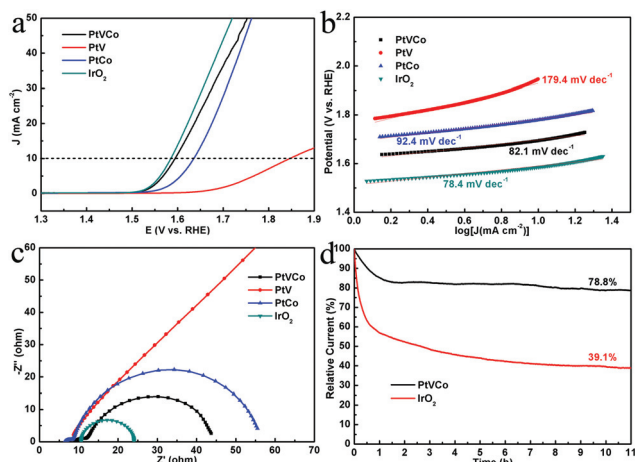

Fig. 4 (a) LSV curves of PtVCo, PtV, PtCo and commercial IrO$_2$ in N$_2$-saturated 1 M KOH solution with a scan rate of 10 mV s^{-1}. (b) Tafel plot of the samples derived from the OER polarization curves. (c) Electrochemical impedance spectra on the RRDE electrode at +1.59 V (vs. RHE) for the OER recorded in 1 M KOH at a rotation rate of 1600 rpm. (d) The chronoamperometric curves of PtVCo and the commercial IrO$_2$ catalyst.
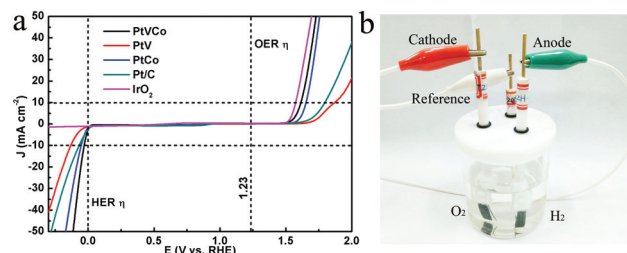

Fig. 5 (a) Combined HER and OER catalytic performance of PtVCo, PtV, PtCo, Pt/C and IrO$_2$ in 1 M KOH at a scan rate of 10 mV s^{-1}. (b) The image of electrocatalytic water electrolysis through the catalysts of PtVCo coated on a carbon fiber paper as the anode and cathode in 1 M KOH at an applied potential of +1.70 V (vs. RHE).
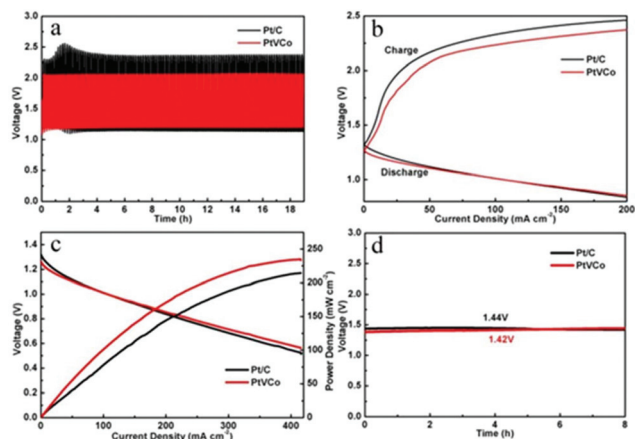
Fig. 6 The performance of PtVCo as the air-cathode in a home-made Zn–air battery: (a) cycling performance of the rechargeable Zn–air battery using PtVCo at 10 mA cm^{-2} compared with commercial Pt/C. (b) Charge and discharge polarization curves of the rechargeable Zn–air battery using PtVCo compared with Pt/C. (c) Polarization and power density curves of the Zn–air batteries of the PtVCo and Pt/C catalysts. (d) Open-circuit potential sketch of PtVCo and commercial Pt/C.

curves revealed that PtVCo displayed an onset potential of 0.89 V, more positive than that of PtV and PtCo and nearly identical to that of Pt/C. Moreover, PtVCo showed a kinetic current density of 3.2 mA cm^{-2}, much higher than that of PtV, PtCo and Pt/C as well.

Inspired by the excellent performance toward the OER for PtVCo, a self-made zinc–air battery (ZAB) was assembled to explore the possibility of PtVCo as the air-cathode (Fig. S5†). Fig. 6a shows the undulating charge voltage of PtVCo and Pt/C. After a continuous galvanostatic charge–discharge test for over 18 hours, the charge–discharge voltage gap of PtVCo remained at about 0.88 V, much lower than that of Pt/C (1.23 V), indicating a superior performance. Fig. 6b presents the charge and discharge polarization curves of the two-electrode battery with Pt/C and PtVCo as the air-cathodes. In addition, the discharge voltage curve and the corresponding power density are depicted in Fig. 6c. PtVCo displayed a maximal power density of 235 mW cm^{-2}, much higher than that of Pt/C (215 mW cm^{-2}). Finally, the open-circuit potential plot of PtVCo and Pt/C can be found in Fig. 6d. The approximate open circuit potential of PtVCo is 1.42 V, close to that of Pt/C (1.44 V). Overall, PtVCo demonstrated high promise for cost-effective and stable electrodes for high power ZAB applications superior to Pt/C.

Conclusions

In summary, PtVCo alloys with well-defined dendrite structures have been fabricated to catalyze the HER and OER with high efficiency. In alkaline electrolytes, the HER performance was superior to that of Pt/C and the OER activity was close to that of IrO$_2$, and such excellent bifunctional electrocatalytic performance enabled PtVCo to catalyze overall water splitting

very efficiently. In addition, in the rechargeable Zn–air battery test, a charge–discharge voltage gap of 0.88 V and a maximal power density of 235 mW cm^{-2} were demonstrated for PtVCo, mainly attributable to the additional synergistic effects from Pt, V and Co. The findings here may pave a pathway for rational design of advanced multifunctional electrodes toward renewable energy devices and beyond.

Conflicts of interest

There are no conflicts to declare.

Acknowledgements

References

1 J. Mahmood, F. Li, S.-M. Jung, M. S. Okyay, I. Ahmad, S.-J. Kim, N. Park, H. Y. Jeong and J.-B. Baek, *Nat. Nanotechnol.*, 2017, **12**, 441–446.
2 J. Su, Y. Yang, G. Xia, J. Chen, P. Jiang and Q. Chen, *Nat. Commun.*, 2017, **8**, 14969.
3 J. Yin, Q. Fan, Y. Li, F. Cheng, P. Zhou, P. Xi and S. Sun, *J. Am. Chem. Soc.*, 2016, **138**, 14546–14549.
4 Y. Xu, M. Kraft and R. Xu, *Chem. Soc. Rev.*, 2016, **45**, 3039–3052.
5 W. Wang, X. Xu, W. Zhou and Z. Shao, *Adv. Sci.*, 2017, **4**, 1600371.
6 M. I. Jamesh, *J. Power Sources*, 2016, **333**, 213–236.
7 Y. Li and J. Lu, *ACS Energy Lett.*, 2017, **2**, 1370–1377.
8 J. Yin, Y. Li, F. Lv, Q. Fan, Y.-Q. Zhao, Q. Zhang, W. Wang, F. Cheng, P. Xi and S. Guo, *ACS Nano*, 2017, **11**, 2275–2283.
9 Y. Li and H. Dai, *Chem. Soc. Rev.*, 2014, **43**, 5257–5275.
10 J. Yin, Y. Li, F. Lv, M. Lu, K. Sun, W. Wang, L. Wang, F. Cheng, Y. Li, P. Xi and S. Guo, *Adv. Mater.*, 2017, **29**, 1704681.
11 Y. Guo, P. Yuan, J. Zhang, Y. Hu, I. S. Amiinu, X. Wang, J. Zhou, H. Xia, Z. Song, Q. Xu and S. Mu, *ACS Nano*, 2018, **12**, 1894–1901.
12 W. Niu, S. Pakhira, K. Marcus, Z. Li, J. L. Mendoza-Cortes and Y. Yang, *Adv. Energy Mater.*, 2018, **8**, 1800480.
13 W. Niu, Z. Li, K. Marcus, L. Zhou, Y. Li, R. Ye, K. Liang and Y. Yang, *Adv. Energy Mater.*, 2018, **8**, 1701642.
14 M. Zhang, Q. Dai, H. Zheng, M. Chen and L. Dai, *Adv. Mater.*, 2018, **30**, 1705431.

15 T. Ma, C. Li, X. Chen, F. Cheng and J. Chen, *Inorg. Chem. Front.*, 2017, **4**, 1628–1633.

16 D. Strmcnik, P. P. Lopes, B. Genorio, V. R. Stamenkovic and N. M. Markovic, *Nano Energy*, 2016, **29**, 29–36.

17 Z. Tang, W. Wu and K. Wang, *Catalysts*, 2018, **8**, 65–82.

18 P. Strasser, *Acc. Chem. Res.*, 2016, **49**, 2658–2668.

19 J. Wang, H. Zhang and X. Wang, *Small Methods*, 2017, **1**, 1700118.

20 R. R. Rao, M. J. Kolb, N. B. Halck, A. F. Pedersen, A. Mehta, H. You, K. A. Stoerzinger, Z. Feng, H. A. Hansen, H. Zhou, L. Giordano, J. Rossmeisl, T. Vegge, I. Chorkendorff, I. E. L. Stephens and Y. Shao-Horn, *Energy Environ. Sci.*, 2017, **10**, 2626–2637.

21 K. Liang, L. Guo, K. Marcus, S. Zhang, Z. Yang, D. E. Perea, L. Zhou, Y. Du and Y. Yang, *ACS Catal.*, 2017, **7**, 8406–8412.

22 Z. Li, W. Niu, L. Zhou and Y. Yang, *ACS Energy Lett.*, 2018, **3**, 892–898.

23 Q. Zhao, Z. Yan, C. Chen and J. Chen, *Chem. Rev.*, 2017, **117**, 10121–10211.

24 D. Yang, L. Zhang, X. Yan and X. Yao, *Small Methods*, 2017, **1**, 1700209.

25 C. Wang, N. M. Markovic and V. R. Stamenkovic, *ACS Catal.*, 2012, **2**, 891–898.

26 W. Wang, B. Lei and S. Guo, *Adv. Energy Mater.*, 2016, **6**, 1600236.

27 L. Bu, S. Guo, X. Zhang, X. Shen, D. Su, G. Lu, X. Zhu, J. Yao, J. Guo and X. Huang, *Nat. Commun.*, 2016, **7**, 11850.

28 G. Greco, A. Witkowska, M. Minicucci, L. Olivi, E. Principi, S. Dsoke, A. Moretti, R. Marassi and A. Di Cicco, *J. Phys. Chem. C*, 2012, **116**, 12791–12802.

29 J. Wu, S. Shan, J. Luo, P. Joseph, V. Petkov and C.-J. Zhong, *ACS Appl. Mater. Interfaces*, 2015, **7**, 25906–25913.

30 R. Loukrakpam, S. Shan, V. Petkov, L. Yang, J. Luo and C.-J. Zhong, *J. Phys. Chem. C*, 2013, **117**, 20715–20721.

31 B. N. Wanjala, B. Fang, S. Shan, V. Petkov, P. Zhu, R. Loukrakpam, Y. Chen, J. Luo, J. Yin, L. Yang, M. Shao and C.-J. Zhong, *Chem. Mater.*, 2012, **24**, 4283–4293.

32 B. Fang, J. Luo, P. N. Njoki, R. Loukrakpam, B. Wanjala, J. Hong, J. Yin, X. Hu, J. Last and C.-J. Zhong, *Electrochim. Acta*, 2010, **55**, 8230–8236.

33 Z. Guo, X. Dai, Y. Yang, Z. Zhang, X. Zhang, S. Mi, K. Xu and Y. Li, *J. Mater. Chem. A*, 2013, **1**, 13252–13260.

34 P. Kolla and A. Smirnova, *Electrochim. Acta*, 2015, **182**, 20–30.

35 R. Sriphathoorat, K. Wang, S. Luo, M. Tang, H. Du, X. W. Du and P. K. Shen, *J. Mater. Chem. A*, 2016, **4**, 18015–18021.

36 N. Zhang, L. Bu, S. Guo, J. Guo and X. Huang, *Nano Lett.*, 2016, **16**, 5037–5043.

37 Y.-L. Zhang, W.-J. Shen, W.-T. Kuang, S. Guo, Y.-J. Li and Z.-H. Wang, *ChemSusChem*, 2017, **10**, 2375–2379.

38 L. Bu, N. Zhang, S. Guo, X. Zhang, J. Li, J. Yao, T. Wu, G. Lu, J.-Y. Ma, D. Su and X. Huang, *Science*, 2016, **354**, 1410–1414.

39 T. Mitsudome, K. Miyagawa, Z. Maeno, T. Mizugaki, K. Jitsukawa, J. Yamasaki, Y. Kitagawa and K. Kaneda, *Angew. Chem., Int. Ed.*, 2017, **56**, 9381–9385.

40 W. He, J. Cai, H. Zhang, L. Zhang, X. Zhang, J. Li and J.-J. Yin, *ACS Appl. Nano Mater.*, 2018, **1**, 222–231.

41 L. Wang, Z. Tang, W. Yan, Q. Wang, H. Yang and S. Chen, *J. Power Sources*, 2017, **343**, 458–466.

42 P. Bera, K. R. Priolkar, A. Gayen, P. R. Sarode, M. S. Hegde, S. Emura, R. Kumashiro, V. Jayaram and G. N. Subbanna, *Chem. Mater.*, 2003, **15**, 2049–2060.

43 S. Bai, C. Wang, M. Deng, M. Gong, Y. Bai, J. Jiang and Y. Xiong, *Angew. Chem., Int. Ed*, 2014, **53**, 12120–12124.

44 G. Silversmit, D. Depla, H. Poelman, G. B. Marin and R. D. Gryse, *J. Electron Spectrosc. Relat. Phenom.*, 2004, **135**, 167–175.

45 H. Jin, J. Wang, D. Su, Z. Wei, Z. Pang and Y. Wang, *J. Am. Chem. Soc.*, 2015, **137**, 2688–2694.

46 N. Wang, L. Li, D. Zhao, X. Kang, Z. Tang and S. Chen, *Small*, 2017, **13**, 1701025.

47 D. Li, Z. Zong, Z. Tang, Z. Liu, S. Chen, Y. Tian and X. Wang, *ACS Sustainable Chem. Eng.*, 2018, **6**, 5105–5114.

48 N. Weidler, S. Paulus, J. Schuch, J. Klett, S. Hoch, P. Stenner, A. Maljusch, J. Brotz, C. Wittich, B. Kaiser and W. Jaegermann, *Phys. Chem. Chem. Phys.*, 2016, **18**, 10708–10718.

49 A. Ullman, Y. Liu, M. Huynh, D. K. Bediako, H. Wang, B. L. Anderson, D. C. Powers, J. J. Breen, H. D. Abruña and D. G. Nocera, *J. Am. Chem. Soc.*, 2014, **136**, 17681–17688.

50 D.-H. Ha, B. Han, M. Risch, L. Giordano, K. P. C. Yao, P. Karayaylali and Y. Shao-Horn, *Nano Energy*, 2016, **29**, 37–45.

51 V. Maruthapandian, M. Mathankumar, V. Saraswathy, B. Subramanian and S. Muralidharan, *ACS Appl. Mater. Interfaces*, 2017, **9**, 13132–13141.